Energy and AI 14 (2023) 100261

Contents lists available at ScienceDirect

Energy and AI

journal homepage: www.sciencedirect.com/journal/energy-and-ai

Integration of multi-physics and machine learning-based surrogate modelling approaches for multi-objective optimization of deformed GDL of PEM fuel cells

Jiankang Wang [a,#], Hai Jiang [b,#], Gaojian Chen [b], Huizhi Wang [c], Lu Lu [d], Jianguo Liu [a,e,*], Lei Xing [f,*]

[a] National Laboratory of Solid-State Microstructures, College of Engineering and Applied Sciences, Nanjing University, Nanjing, 210093, China
[b] School of chemistry and chemical engineering, Jiangsu University, Zhenjiang, 212013, China
[c] Department of Mechanical Engineering, Imperial College London, London SW7 2BX, UK
[d] Department of Chemical and Biomolecular Engineering, University of Pennsylvania, Philadelphia PA 19104, USA
[e] Institute of Energy Power Innovation, North China Electric Power University, Beijing 102206, China
[f] Department of Chemical and Process Engineering, University of Surrey, Guildford GU2 7XH, UK

HIGHLIGHTS

- Five key GDL parameters on PEMFC performance and oxygen homogeneity are studied.
- Multi-physics and data-driven models are integrated for multi-objective optimization.
- Two data-driven models, RSM and ANN, are developed and compared.
- Cell performance and oxygen homogeneity are remarkably improved after optimization.
- Trade-off of current density and standard deviation of oxygen distribution is revealed.

GRAPHICAL ABSTRACT

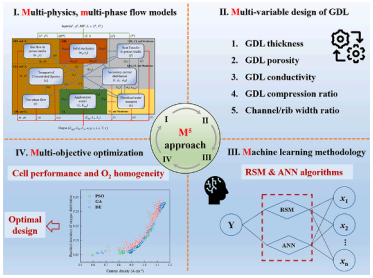

ARTICLE INFO

Keywords:
Multi-physics modelling
Machine learning
Multi-objective optimization
Gas diffusion layer
Proton exchange membrane fuel cells

ABSTRACT

The development of artificial intelligence (AI) greatly boosts scientific and engineering innovation. As one of the promising candidates for transiting the carbon intensive economy to zero emission future, proton exchange membrane (PEM) fuel cells has aroused extensive attentions. The gas diffusion layer (GDL) strongly affects the water and heat management during PEM fuel cells operation, therefore multi-variable optimization, including thickness, porosity, conductivity, channel/rib widths and compression ratio, is essential for the improved cell performance. However, traditional experiment-based optimization is time consuming and economically

Abbreviations: AI, artificial intelligent; ANN, artificial neural network; BBD, Box-Behnken Design; CL, catalyst layer; CR, compression ratio; DE, differential evolution; DoE, design of experiment; EOD, electro-osmotic drag; FEM, finite element method; GA, genetic algorithm; GDE, gas diffusion electrode; GDL, gas diffusionlayer; GSA, global sensitivity analysis; HOR, hydrogen oxidation reaction; LOO, leave-one-out; MPL, micro porous layer; ORR, oxygen reduction reaction; PDE, partial differential equation; PEM, proton exchange membrane; PSO, particle swarm optimization algorithm; RSM, Response surface methodology; TPBs, triple phase boundaries.

* Corresponding authors.
E-mail addresses: jianguoliu@nju.edu.cn (J. Liu), l.xing@surrey.ac.uk (L. Xing).
# The two authors contributed equally to this work.

https://doi.org/10.1016/j.egyai.2023.100261

Available online 6 April 2023

unaffordable. To break down the obstacles to rapidly optimize GDLs, physics-based simulation and machine-learning-based surrogate modelling are integrated to build a sophisticated M^5 model, in which multi-physics and multi-phase flow simulation, machine-learning-based surrogate modelling, multi-variable and multi-objects optimization are included. Two machine learning methodologies, namely response surface methodology (RSM) and artificial neural network (ANN) are compared. The M^5 model is proved to be effective and efficient for GDL optimization. After optimization, the current density and standard deviation of oxygen distribution at 0.4 V are improved by 20.8% and 74.6%, respectively. Pareto front is obtained to trade off the cell performance and homogeneity of oxygen distribution, e.g., 20.5% higher current density is achieved when sacrificing the standard deviation of oxygen distribution by 26.0%.

1. Introduction

As a highly effective and environmentally friendly energy conversion device, proton exchange membrane (PEM) fuel cells are considered as promising candidates of transiting the carbon intensive economy to zero emission future [1–3]. With the rapid development of computer and data science and engineering, multi-physics and multi-phase flow models, along with experimental validation, are widely used in diagnosing, predicting and optimizing PEM fuel cells [4]. In recent years, machine learning and artificial intelligent (AI) exhibited strong power in the R&D of materials and energy, e.g., the physics-informed neural networks for machine-learning fluid flow recently proposed by Raissi et al. [5]. Machine learning and AI have great potential to accelerate the development of the state-of-the-art PEM fuel cell technology through significantly reducing cost and improving performance and durability [6].

Although time and resources could be significantly reduced using complex physical models, e.g., the multi-physics and multi-phase flow models, the computational and time costs are still unaffordable when solving partial differential equations (PDEs) over a complex geometry, e.g., few days or weeks are required to solve a 3D steady-state small fuel cell stack model discretized into less than 100 million nodes of grid [7–9]. In this regard, a feasible approach is to train the machine learning and AI model by a certain number of data obtained from the complex physical models, that typically refers to data-driven surrogate modelling. Data-driven surrogate models have been applied to predict PEM fuel cell performance in steady-state and dynamic conditions [10,11], screen catalyst materials [12,13], optimize electrode composition [14,15], and assist the development of control strategies to maximize the cell performance and mitigate material degradation [16,17]. With respect to learning style, machine learning algorithms could be generally categorized into supervised learning, unsupervised learning, and reinforcement learning [6]. Amongst them, Gaussian process based artificial neural network (ANN) achieves good performance with the support of big data and complex physics. Moreover, there are also several statistics-based data-driven models and approaches. Response surface methodology (RSM) explores the statistic relationships between several explanatory variables and one or more response variables through high-degree polynomial regressions, that has been applied in commercial software, e. g. ANSYS Fluent [18,19]. In comparison with machine learning methods, e.g., ANN, the statistic-based methods, e.g., RSM and Kriging focus on regression instead of classification, leading to a relatively simple algorithms and low requirement of massive training data, however, less suitability for the optimization problems involved a large number of design variables [20].

In PEM fuel cells, gas diffusion electrode (GDE), consisted of catalyst layer (CL), gas diffusion layer (GDL) and micro porous layer (MPL), is the core of PEM fuel cell, in which several functional components interacted to construct triple phase boundaries (TPBs) and the overall cell performance is mainly determined by the fully coupled electrochemical reaction in the CL and the transport processes of mass, species, charge and heat in all domains. The pioneering multi-variable optimization of porous electrode could be traced back to the work of Secanell et al. [21], in which the agglomerate model developed by Sun et al. [22] was coupled with objective functions and constrains to optimize four parameters, i.e., platinum loading, Pt/C ratio, volume fraction of ionomer inside the agglomerate and porosity of GDL, to maximum the cell performance. In their later work [23], the production costs were added as a new optimization objective. Five design variables, i.e., platinum loading, Pt/C ratio, agglomerate radius, ionomer film thickness and ionomer volume fraction inside the agglomerate, were investigated. It was suggested that minimum platinum loading at the anode is a practical strategy to significantly reduce the cost with very little penalty in performance. As a follow-up, the fuel cell model was coupled with a gradient-based optimization algorithm implemented in DAKOTA to study the optimal platinum loading, Pt/C ratio, ionomer volume fraction inside agglomerates and GDL porosity at three different operating cell voltages [24]. Khajeh-Hosseini-Dalasm et al. [25] comprehensively studied eight structural parameters, including platinum loading, carbon loading, ionomer volume fraction, CL thickness, GDL porosity, agglomerate radius, ionomer film thickness et al., based on the steady-state one-dimensional agglomerate model. Xing et al. [26] applied surrogate model and global sensitivity analysis (GSA) to evaluate the optimal values of five CL variables, i.e., platinum loading, Pt/C mass ratio, ionomer volume fraction, CL thickness and agglomerate size, at a given cell voltage and a range of cell voltages, respectively, representing three typical current density ranges from low to high. Wang et al. [27] integrated a three-dimensional CFD fuel cell model with an AI-based data-driven surrogate model and an optimization framework to realize the multi-variable global optimization of CL composition for improving the maximum power density. Ding et al. [28] built a data-driven surrogate model to optimize the catalyst loading and ionomer content with the aim of improving Pt utilization. In their work, eight machine leaning algorithms were compared and ANN achieved the best prediction accuracy. It is widely accepted that a comprehensive physical model, after experimental validation, lays the foundation of data-driven surrogate model because the data used for machine leaning model training is the output of the physical model. Thus, the more processes could be taken into account in a physical model, the higher reliability of the generated database for machine learning model training. In most previous electrode composition optimization models, simplified physical models, e.g., single phase flow [21,23-26], isothermal assumption [25], one-dimensional geometry [28], were developed. However, more comprehensive multi-physics and two-phase flow models are required to account for the influence of multiple processes on the modelling results, e.g., the formation of liquid water and the associated impact on gas transport, the non-uniform variation of electrode porosity owing to clamping force et al. Although CL optimization has been focused in many previous works, a comprehensive surrogate modelling of GDL has rarely been commenced.

Data-driven surrogate models are advantageous in computational efficiency and taking into account the effects of physics that have not been yet revealed by physical models, but strongly constrained by training data. ANN is suitable for predicting the time-dependant cell performance, especially for long-term operation when degradation is a concern. The accuracy of the ANN models is highly dependant on the number of data, for example, the adaptive neuro-fuzzy inference system (ANFIS) that has been successfully used for time-series prediction of

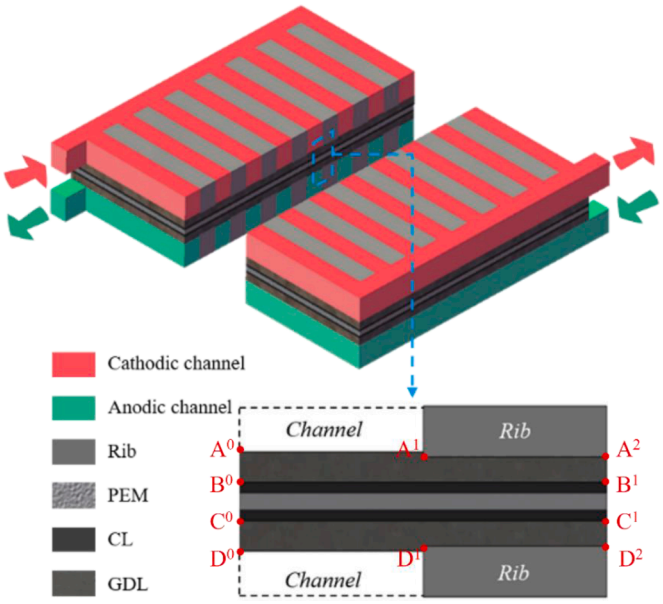

Fig. 1. Sketch of the PEMFC unit and the modelling domain.

voltage decay caused by electrode degradation, thanks to its gradient-boosted regression capabilities [29]. Although ANN models can handle complex physics with many design variables supported by massive training data, they may not be the best choice for scenarios with fewer design variables. In such cases, simpler statistical methods like RSM are often considered superior to ANN. RSM has the advantage of producing polynomial expressions that reflect the combined effects of design variables. These analytical expressions can then be easily integrated into higher-level models, such as system-level models. Moreover, the accuracy and precision of data-driven models are strongly determined by the physical models.

In this work, physics-based simulation and machine-learning-based surrogate modelling are integrated to build a sophisticated M^5 model, in which multi-physics and multi-phase flow simulation, machine-learning-based surrogate modelling are included, to perform multi-variable and multi-objects optimization of the GDL of PEMFCs. Firstly, we developed a comprehensive multi-physics, two-phase flow, non-isothermal model to describe the detailed electrochemical and physical processes in a PEM fuel cell. The multi-variable optimization of five GDL properties related variables, including compression ratio (*CR*), channel/rib width ratio, porosity, thickness, and electrical conductivity, are investigated. The developed physical model is then validated by experimental results and used to generate a certain amount of data for the data-driven surrogate model. Two data-driven approaches, including RSM and ANN, are compared with respect to required amount of data for training and prediction accuracy. Current density and the oxygen distribution homogeneity are chosen as two objectives and their trade-offs are presented by Pareto front. Corresponding combinations of the studied five parameters are obtained to achieve the optimal cell performance. The M^5 model developed in this work can effectively and efficiently optimize the GDL, with a great potential in investigating and optimizing other complex electrochemical systems.

2. Model descriptions

2.1. Model development

In this work, a two-dimensional, across-the-channel, multi-physics, two-phase model, based on the geometry as shown in Fig. 1, was propounded to investigate the variation in cell performance of a PEM fuel cell caused by the non-uniform deformation of GDLs that took place due to the special channel-rib pattern of the flow field under different degree of clamping force. The modelling domain consisted of two GDLs, two CLs and a PEM. The model is well validated with experimental data in our previous paper [30]. And then, RSM and ANN model were designed and solved to optimize the physical parameters of GDLs to maximize the cell performance of the cell and homogenize the oxygen profile within the cathode electrode.

The overall main assumption of the model as follows:

1 PEM fuel cell is operated in steady-state;
2 The reactant gases are treated as ideal gases and the reactant flow is treated as laminar;
3 The PEM is impermeable to any gases, only water and proton migration is allowed;
4 Only the deformation of GDL is considered and the deformation is elastic.

2.2. Governing equation

2.2.1. Conservation of mass

Maxwell-Stefan formulation is applied to describe the mass balance and transport through diffusion and convection inside the porous media, GDL and CL.

$$\nabla\left\{-\rho\omega_i\sum_j D_{ij}^{eff}\left[\frac{M_n}{M_j}\left(\nabla\omega_j+\omega_j\frac{\nabla M_n}{M_n}\right)+\left(x_j-\omega_j\right)\frac{\nabla P}{P}\right]+\rho u\omega_i\right\}=R_i \tag{1}$$

where ρ and P are the density and pressure of the gas mixture; ω, x, M and M_n represent the mass fraction, molar fraction, molar mass and mean molar mass, respectively. R is the source term. D_{ij}^{eff} is the effective binary diffusivity of species i and j, which can be contained by the Bruggeman correlation as following [31]:

$$D_{ij,a}^{eff}=\varepsilon_k^{1.5}D_{ij} \tag{2}$$

$$D_{ij,c}^{eff}=\left[(1-s)\varepsilon_k\right]^{1.5}D_{ij} \tag{3}$$

where a and c represent the anode and cathode; k represents the different porous media, GDL and CL; ε is the porosity and D_{ij} is the Maxwell-Stefan diffusivity matrix. s is the water saturation, defined as the volume fraction of void space occupied by liquid water. where u^g is the velocity of the reactant gases in porous media can be expressed by the Darcy's law.

$$u^g=-\frac{K_p}{\mu^g}\nabla P \tag{4}$$

where K_p represents the permeability of the porous media; μ^g is the viscosity of the gas mixture.

2.2.2. Conservation of charge

Proton transport in the electrolyte (ionomer) phase and the electron transport in the solid phase in the catalyst layers (CLs) are described by the charge conservation equation, which is written below:

$$\nabla\left(-\sigma_m^{eff}\nabla\phi_m\right)+\nabla\left(-\sigma_s^{eff}\nabla\phi_s\right)=0 \tag{5}$$

where ϕ_m and ϕ_s are the electrolyte and electrode phase potential, respectively. σ_m^{eff} and σ_s^{eff} are the effective ionic and electronic conductivities in the porous media, respectively. The effective conductivities are corrected using the Bruggeman formula [31] and the effective ionic conductivity in cathode catalyst layer (CCL) is modified by the equation developed by Kamarajugadda and Mazumder [32].

$$\sigma_m^{eff} = \begin{cases} \sigma_m & PEM \\ L_m^{1.5}\sigma_m & ACL \\ \left(1-\varepsilon_{CL}^0\right)\left[1+\dfrac{\left(\varepsilon_{agg}-1\right)}{\left(1+\delta_m/r_{agg}+a_0\right)}\right]\sigma_m & CCL \end{cases} \tag{6}$$

$$\sigma_s^{eff} = \begin{cases} \left(1-\varepsilon_{GDL}^0\right)^{1.5}\sigma_s & GDL \\ \left(1-\varepsilon_{CL}^0-L_M\right)^{1.5}\sigma_s & CL \end{cases} \tag{7}$$

where ε_{agg} is the volume fraction of ionomer in agglomerate; δ_m is the thickness of the ionomer film; r_{agg} is the radius of agglomerate; L_m represents the volume fraction of the ionomer; ε^0 is the original porosity of the porous media and a_0 is a dimensionless parameter, which is given by:

$$a_0 = \min\left[0, \left(\frac{\delta_m}{r_{agg}} + \left(1-\varepsilon_{agg}\right)^{1/3} - 1\right)\right] \tag{8}$$

The intrinsic ionic conductivity, σ_m, is a function of the operating temperature and water content, which can be expressed as [33]:

$$\sigma_m = (0.5139\lambda - 0.326)\exp\left[1268\left(\frac{1}{303}-\frac{1}{T}\right)\right] \tag{9}$$

2.2.3. Dissolved-water transport through the membrane

Dissolved-water transport through the membrane includes three mechanisms: electro-osmotic drag (EOD) of water molecules carried by protons migrating from anode to cathode, hydraulic permeation caused by the pressure gradient and back diffusion driven by the concentration gradient of water. A second order partial differential equation (PDE) is developed to describe the process [34].

$$\nabla\cdot\left(n_d\frac{i_m}{F}\right) - \nabla\cdot\left(D_W^m\nabla c_W^d\right) - \nabla\cdot\left(\frac{k_p^m c_W^d}{\mu_W}\nabla P\right) = S_W^d \tag{10}$$

where n_d represents the EOD coefficient, which is expressed as $2.5\lambda/22$, i_m is the electrolyte current density, $F$is the Faraday's constant, k_p^m is the membrane permeability, μ_W is the water viscosity, S_W^d is the source term of the dissolved water. D_W^m is the diffusivity of dissolved water in the membrane, which is a piecewise function determined by operating temperature and membrane water content as follow [35]:

$$D_W^m = \begin{cases} D_0\left(2.563 - 0.33\lambda + 0.0264\lambda^2 - 0.000671\lambda^3\right) & \lambda > 4 \\ D_0\left(-1.25\lambda + 6.65\right) & 3 < \lambda \le 4 \\ D_0\left(2.05\lambda - 3.25\right) & 2 \le \lambda \le 3 \end{cases} \tag{11}$$

$$D_0 = 1.0\times10^{-10}\exp\left[2416\left(\frac{1}{303}-\frac{1}{T}\right)\right] \tag{12}$$

The concentration of the dissolved water, c_W^d, is a function of the water content of the membrane and ionomer, as following [33]:

$$c_W^d = \frac{\rho_m}{EW}\frac{\lambda}{1+k_s\lambda} \tag{13}$$

where ρ_m is the density of dry membrane, $EW$is the equivalent weight of membrane, k_s is the swelling coefficient, which is used to describe the volume increase of the membrane and ionomer. The water content, λ, is described as a function of water activity:

$$\lambda = \begin{cases} 0.043 + 17.81\alpha_W - 39.85\alpha_W^2 + 36.0\alpha_W^3 & \alpha_W < 1 \\ 14.0 + 1.4(\alpha_W - 1) & 1 \le \alpha_W \le 3 \\ 16.8 & \alpha_W > 3 \end{cases} \tag{14}$$

$$\alpha_W = x_W\frac{P_{op}}{P_W^{sat}} + 2s \tag{15}$$

where P_{op} is the operating pressure, P_W^{sat} represents the water saturation pressure, which is calculated empirically as [33]:

$$P_{sat} = \begin{array}{l} 9.531\times10^{-4}(T-237)^4 - 3.123\times10^{-2}(T-237)^3 + \\ 3.451(T-237)^2 + 20.96(T-237) + 611.0 \end{array} \tag{16}$$

2.2.4. Liquid water transport in the porous media

The transport of the liquid water in the porous media is expressed using the following equation [31]:

$$\nabla\cdot\left(\rho_W^l D_c\nabla s - \frac{\rho_W^l k_r^l \mu_W^g}{k_r^g \mu_W^l}u^g\right) = M_W S_W^l \tag{17}$$

where ρ_W^l is the density of liquid water, μ_W^g and k_r^g are the viscosity and relative permeability of gas phase, respectively. μ_W^l and k_r^l are the viscosity and relative permeability of liquid phase, respectively. M_W is the molecular weight of water, S_W^l is the source term of the liquid water. D_c is the capillary diffusion coefficient defined as:

$$D_c = -\frac{k_r^l}{\mu_W^l}\frac{dP_c}{ds} \tag{18}$$

where P_c is the capillary pressure, defined as the difference pressure between the water vapour and liquid water, which is calculated using the following expression [36]:

$$P_c = \sigma\cos(\theta_c)\left(\frac{\varepsilon^0}{K_p}\right)^{1/2}J(s) \tag{19}$$

where σ is the liquid-gas surface tension (0.0625 N/m), θ_c is the contact angle between the liquid droplets and the solid surface, $J(s)$is the Leverett function [36], which is given by:

$$J(s) = \begin{cases} 1.417(1-s) - 2.120(1-s)^2 + 1.263(1-s)^3 & \theta_c < 90^\circ \\ 1.417s - 2.120s^2 + 1.263s^3 & \theta_c > 90^\circ \end{cases} \tag{20}$$

Combining Eqns. (4 −16), the water saturation, s, can be calculated by the following equation:

$$\rho_W^l D_c\nabla^2 s = M_W S_W^l - \frac{\rho_W^l k_r^l K_P \mu_W^g}{k_r^g \mu_W^l \mu^g}\nabla^2 P \tag{21}$$

The first term on the right side is the water generation rate and the second term on the right side is the water removal rate.

2.2.5. Kinetics of electrochemical reactions

The electrochemical reactions in a PEM fuel cell consist of two main half-cell reactions: hydrogen oxidation reaction (HOR) and oxygen reduction reaction (ORR) that take place in the anode catalyst layer (ACL) and cathode catalyst layer (CCL), respectively. The electrochemical parameters used in our model can be found in our previous paper [30]. The HOR rate and ORR rate are respectively calculated using the Bulter-Volmer (B-V) kinetic equation and the agglomerate model.

$$i_a = i_a^0 a_v\left[\exp\left(\frac{\alpha_a F\eta_a}{RT}\right) - \exp\left(\frac{-\alpha_c F\eta_a}{RT}\right)\right] \tag{22}$$

$$i_c = 4F\frac{P_{O_2}}{H_{O_2}}\left[\frac{1}{E_{agg}k_{agg}} + \frac{\left(r_{agg}+\delta\right)}{a_{agg}r_{agg}D_{O_2}^{eff}}\right]^{-1} \tag{23}$$

$$i_a^0 = i_{0,a}^{ref}\left(\frac{P_{H_2}}{c_{H_2}^{ref}H_{H_2}}\right)^{0.5} \tag{24}$$

where i_a and i_c are the volumetric current densities of the anode and cathode, respectively. i_a^0 is the exchange current density of the HOR under standard conditions, a_v is the active specific surface area, $i_{0,a}^{ref}$ is the reference current density of the HOR, α_a and α_c are the anodic and

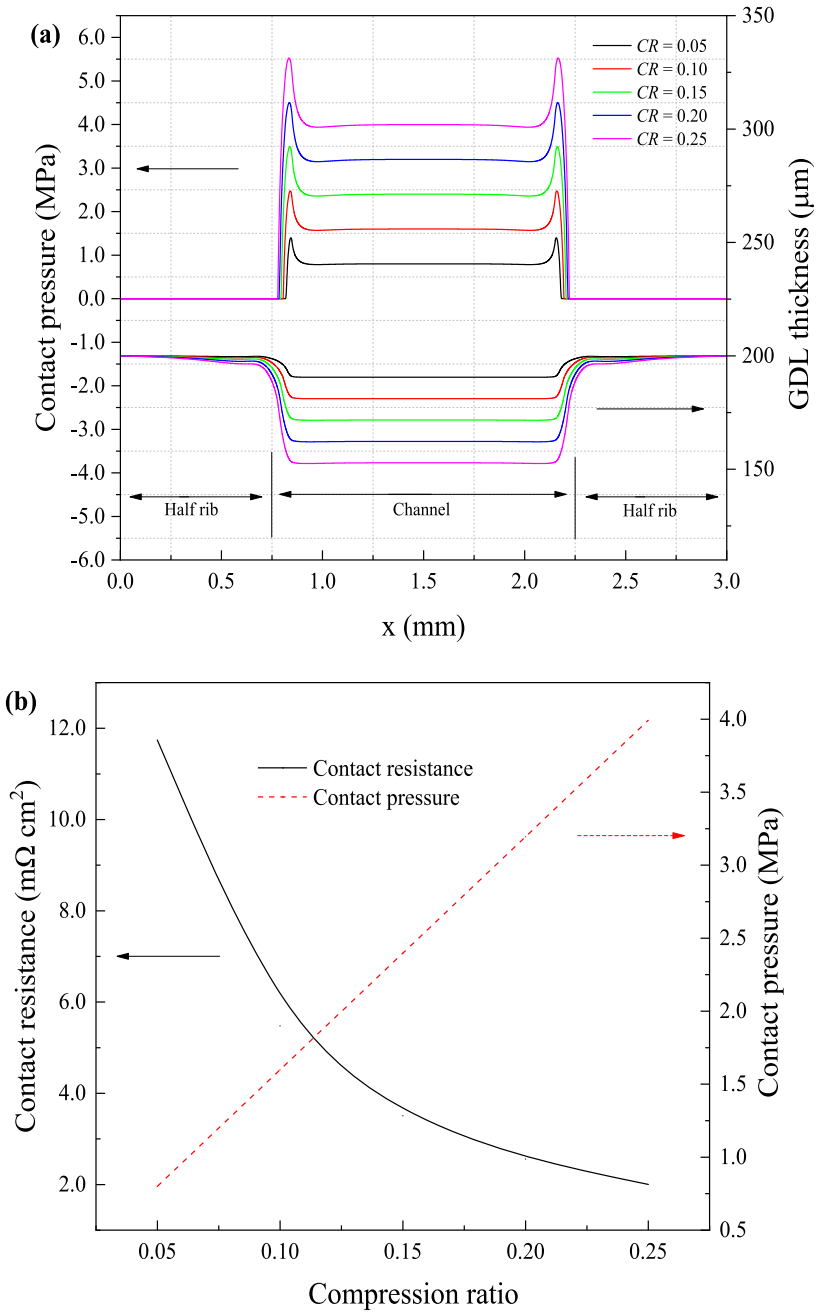

Fig. 2. Profiles of (a) contact pressure and GDL thickness and (b) contact resistance and contact pressure under different compression ratios.

cathodic transfer coefficient, $c_{H_2}^{ref}$ is the reference molar concentration of hydrogen, H_{H_2} and H_{O_2} are the Henry's constant of the hydrogen and oxygen, respectively. P_{H_2} and P_{O_2} are the partial pressure of the hydrogen and oxygen, respectively. δ represents the total thickness of the ionomer film and liquid water film, E_{agg} is the effectiveness factor of the spherical agglomerate [37], which is used to describe the mass transport within the agglomerate as following:

$$E_{agg} = \frac{1}{M_{T,agg}}\left[\frac{1}{\tanh\left(3M_{T,agg}\right)} - \frac{1}{3M_{T,agg}}\right] \tag{25}$$

where $M_{T,agg}$ is a dimensionless parameter named Thiele's modules [37]:

$$M_{T,agg} = \frac{r_{agg}}{3}\sqrt{\frac{k_{agg}}{D_{O_2}^{eff}}} \tag{26}$$

where $D_{O_2}^{eff}$ is the effective oxygen diffusivity inside the agglomerate, k_{agg} represents the reaction rate coefficient calculated using the B-V equation and Faraday's law, which is expressed as following:

$$k_{agg} = \frac{a_{agg} i_{0,c}^{ref}}{4F c_{O_2}^{ref}}\left[\exp\left(\frac{-\alpha_c F\eta_c}{RT}\right) - \exp\left(\frac{\alpha_a F\eta_c}{RT}\right)\right] \tag{27}$$

where a_{agg} represents the surface area per unit agglomerate volume, $i_{0,c}^{ref}$ is the reference current density of the ORR, $c_{O_2}^{ref}$ is the reference molar concentration of the oxygen, F is the Faraday's constant, R is the molar gas constant, η represents the overpotential expressed as follows:

$$\eta = \phi_s - \phi_m - E^{eq} \tag{28}$$

where E^{eq} is the equilibrium potential of the anode and cathode,

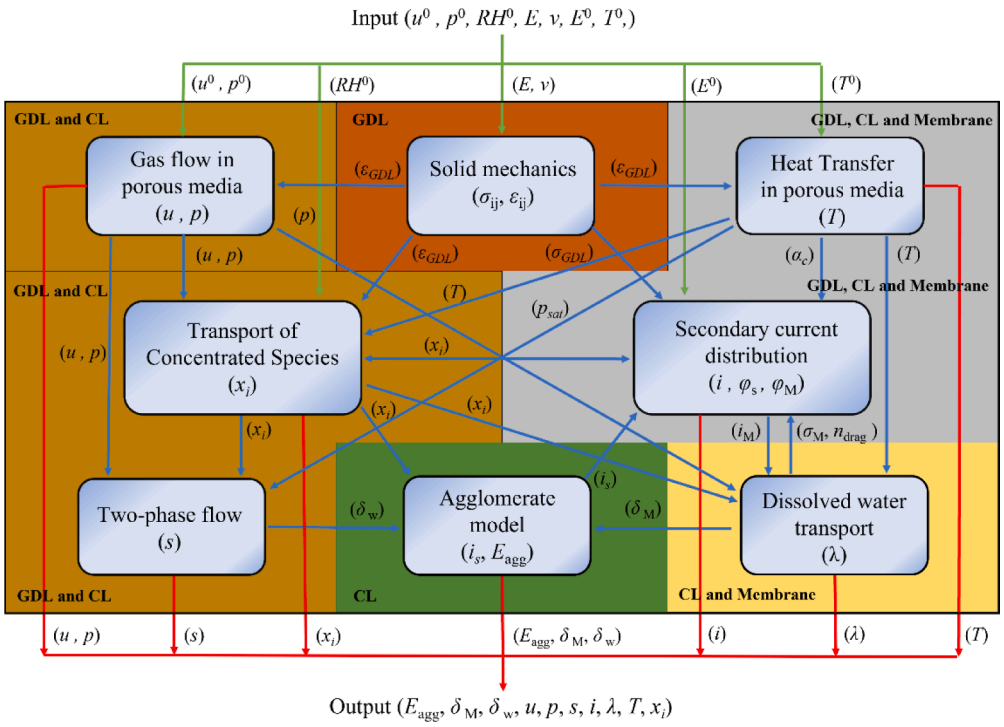

Fig. 3. Schematic of the computational process. Green lines: parameters input; blue lines: model interaction; red lines: model output.

respectively.

2.2.6. Conservation of energy

In this work, all phases are assumed in thermal equilibrium. The heat of this system comes from three parts, which are reaction heat, Joule heat (Ohmic heat) and phase-transfer heat. The multi-phase heat transfer process can be expressed by:

$$\nabla\cdot\left[\sum_{i=g,l}\left(\varepsilon\rho c_p \mathrm{u}\right)_i T\right]-\nabla\cdot\left(\sum_{i=g,l,s}k_i\nabla T\right)=S_T \tag{29}$$

Where the subscript i refers to gas mixture, liquid water and electrode solid phase. The c_p and k_i are specific heat capacity and thermal conductivity, which are decided by the volume fractions of the species within a chosen domain (GDL, CL and membrane/ionomer).

The specific heat capacity and the thermal conductivity of the gas mixture are obtained by using an empirical equation developed by Wike [38]

$$c_p^g=\sum_i x_i c_{p,i}^g, k^g=\sum_i\frac{x_i k_i}{\sum_j x_j\Phi ij} \tag{30}$$

More details could be found elsewhere [39].

2.2.7. Conservation of mass and momentum

In this work, combining the Darcy's law with the continuity equation to govern the conservation of mass and momentum.

$$\frac{\partial}{\partial \mathrm{t}}\left(\rho\varepsilon_p\right)+\nabla\cdot(\rho u)=\mathrm{Q_m} \tag{31}$$

In the above equation, ρ is the fluid density, $\varepsilon_p$is the porosity, and $\mathrm{Q_m}$ is a mass source term. Porosity is defined as the fraction of the control volume that is occupied by pores. Thus, the porosity can vary from zero for pure solid regions to unity for domains of free flow.

2.2.8. Solid mechanics

According to the assumptions, the clamping pressure under different levels of compression ratios can be modelled by the following equations [40]:

$$0=\nabla\cdot\sigma_{ij}+F_V \tag{32}$$

where σ_{ij} is the stress tensor and F_V is the vertical force. The linear relationship between the stress and strain can be described by the Hook's law [40]:

$$\sigma_{ij}=E\cdot\varepsilon_{ij} \tag{33}$$

where E is the Young's modulus and ε_{ij} is the strain.

2.2.9. Contact resistance between GDLs and BPPs

The electrical contact resistance under different clamping pressure between GDLs and BPPs is calculated by the equation from the literature [41].

$$\rho=A\left(\frac{B}{P_{clamp}}\right)^C \tag{34}$$

where P_{clamp} is the clamp pressure between the GDLs and BPPs, A, B, C are empirical constants which is related to the material of the BPPs. The expressions compression ratio and contact resistance as a function of clamping pressure is shown in Fig. 2.

2.3. Boundary conditions

To complete the model, the boundary conditions need to be specified. The operating temperature is fixed as 343.15 K. The GDL-rib interface of the anode (D^1-D^2) is set as a ground with voltage of zero, and the GDL-rib interface of the cathode (A^1-A^2) is set as the operating cell voltage. The initial value of the water content at the CL-GDL interface of the anode (C^0 – C^1) and cathode (B^0 – B^1) are defined as the Dirichlet boundaries, which are expressed by the following equation [42]:

$$\lambda^0=0.043+17.81\alpha_W-39.85\alpha_W^2+36.0\alpha_W^3 \tag{35}$$

where α_W is the water activity, which is a function of the operating

pressure, P, liquid water saturation, s, and the mole fraction of water vapour of the inlet gas mixture, x_w:

$$\alpha_W = x_w \frac{P}{P_{sat}} + 2s \tag{36}$$

The initial inlet concentrations of hydrogen, oxygen, nitrogen and vapour are expressed as following:

$$x^0_{W,a} = \frac{P_{sat} RH^0_a}{P^0_a}, x^0_{H_2} = 1 - x^0_{W,a} \tag{37}$$

$$x^0_{W,c} = \frac{P_{sat} RH^0_c}{P^0_c}, x^0_{O_2} = 0.21\left(1 - x^0_{W,c}\right), x^0_{N_2} = 0.79\left(1 - x^0_{W,c}\right) \tag{38}$$

where pressure (P^0_a and P^0_c), relative humidity (RH^0_a and RH^0_c), and liquid water saturation (s) at the GDL-channel interfaces of the anode ($D^0 - D^1$) and cathode ($A^0 - A^1$) are set as 1 atm, 100% and zero, respectively.

The computational process with the interaction of various parameters is schematically illustrated in Fig. 3.

2.4. Response surface methodology

Response surface methodology (RSM) is a polynomial representation of the mathematical relationship between objectives and research parameters. The general form of RSM based on full quadratic can be expressed as:

$$E_y = \beta_0 + \sum_{i=1}^{m} \beta_i X_i + \sum_{i=1}^{m} \beta_{ii} X_i^2 + \sum_{i<j} \beta_{ij} X_i X_j + \varepsilon \tag{39}$$

Where, the m is the number of parameters, X_i is the parameter i, X_iX_j is the interaction term of each, ε is the residual of the equation, β_0, β_i, β_{ii} and β_{ij} are coefficients of constant term, primary, quadratic, and quadratic interaction terms, respectively. More details about the Factors and their levels for Box-Behnken design and the data is show in the Table S1 and Table S2 in the supporting information (SI).

2.5. Mesh independence

Theoretically, the computation error in the solution related to the grid will disappear for an increasingly fine mesh. The current density at a low cell voltage (0.4 V) was therefore taken as the parameter to evaluate nine mesh grids (shown in Table S3 in the SI) and determine the influence of the element number on the solution. In this study, the number of elements on various computational domains, including flow channel, GDL, CL and membrane, was investigated. In addition, as shown in the Fig S9 in the SI, which is the results of current density and computational duration with different elements, the current density drop become gentle fluctuation when the units of GDLs is over 25. To balance the grid-independent performance and the calculation cost, the Grid 5 was selected as the best griding methods.

2.6. ANN modelling

Artificial neural networks (ANN) are computing systems inspired by the biological neural networks that constitute human brains. An ANN model is a collection of connected units or nodes called artificial neurons. The normalized data of the input parameters X_i will be fed into the first hidden layer through input layer, the artificial neurons of which receive signals then processes them by activate function $f(x)$ after weight them in the connections and can signal neurons connected to it. Therefore, after the nonlinearization process, the outcome of each neurons became a scalar: $f(WXi+b)$. The connections are called edges. The weight increases or decreases the strength of the signal at a connection by the index W. Typically, neurons are aggregated into a sequential architecture, a linear stack of neural layers. Different layers may perform different transformations on their inputs.

After the forward propagation process, the output obtained as the output layer was compared with the real data obtained from the database to compute the difference. In addition, the error was traced backward to retrain the previous neurons and update their parameters. This loop represented the training process and was repeated until the computational values were close enough to real values (training targets).

As the core concept of ANN, backpropagation should be expounded with more detailed mathematical derivations. Suppose that we have a fixed sample set {(x (1), y (1)), …, (x (m), y (m))} which contains m samples. Here we take the most commonly used batch gradient descent method to optimize the neural network. Specifically, for a single sample (x, y), the cost function is:

$$J(W, b; x, y) = \frac{1}{2} \| h_{W,b}(x) - y \|^2 \tag{40}$$

Here we have taken the common variance cost function. Given a data set containing m samples, we can define the overall cost function determined by weights and biases of the neurons as follow (the serial number of sample set was marked with brackets like (x (1), y (1)), the i, j, subscript without brackets represent the i^{th} or j^{th} neuron unit in the first layer):

$$J(W, b) = \left[\frac{1}{m} \sum_{i=1}^{m} \left(\frac{1}{2} \| h_{W,b}\left(x^{(i)}\right) - y^{(i)} \|^2\right)\right] + \frac{\lambda}{2} \sum_{l=1}^{n_l - 1} \sum_{i=1}^{s_l} \sum_{j=1}^{s_1 + 1} \left(W^{(l)}_{ji}\right)^2 \tag{41}$$

Here, the second term was defined as regularization items (also called weight attenuation items) are designed to reduce the magnitude of the weight and prevent overfitting. Weight attenuation parameter λ was used to control the relative importance of two items in the formula. We should notice that these two complex functions are different. $J(W, b; x, y)$ is the variance cost function calculated for a single sample; while $J(W, b)$ is the overall sample cost function, which contains the regularization term. The next step is to minimum the cost function $J(W, b)$ for parameter W and b through the formed optimizers.

To catch the best ANN regression model, the adjustable hyperparameters of ANN algorithms need to be optimized, Common regularization items and dropout layers were introduced as hyperparameters to prevent overfitting. This would ensure that precision could be maintained on the testing data which ANN has never met before. The ANN's topological structure parameters was optimized automatically by default program. Therefore, a six layers sequential model, including an input layer with 5 neural units, two 50-units' neural layers, 2 dropout layers and an output layer with 7 neural units was attained.

2.7. Optimization

Global adaptive search iteration on surrogate models through advanced optimization algorithms such as the genetic algorithm (GA), particle swarm optimization algorithm (PSO) and differential evolution (DE) to find the optimal combination of the 5 parameters and corresponding output values could greatly decrease the workload of the engineering practitioner. Each optimization algorithm has its own peculiarity and an algorithm competition could select one of the first water for specific application scenario. After the algorithm competition, the multi-variable and multi-objective optimization process could be conducted. The scripts are coded on the commercial plat, namely, Jupyter notebook.

2.8. Numerical solution method

The numerical solution of the physics-based models was based on the finite element method (FEM) implemented in commercial software COMSOL Multiphysics 5.6. The spatial and time dependant variables over the computational geometry were obtained through solving the governing equations consisting of several partial differential equations (PDEs). The MUMPS steady-state solver was adopted with default

Table 1
Design variables and boundary values.

Parameter	Level		
	-1	Base-case	1
CR	0.05	0.2	0.25
ε^0_{GDL}	0.5	0.78	0.9
S_r	0.5	1.0	1.5
δ^0_{GDL}(μm)	100	200	400
σ^0_{GDL}(S m^{-1})	5000	12,113	95,000

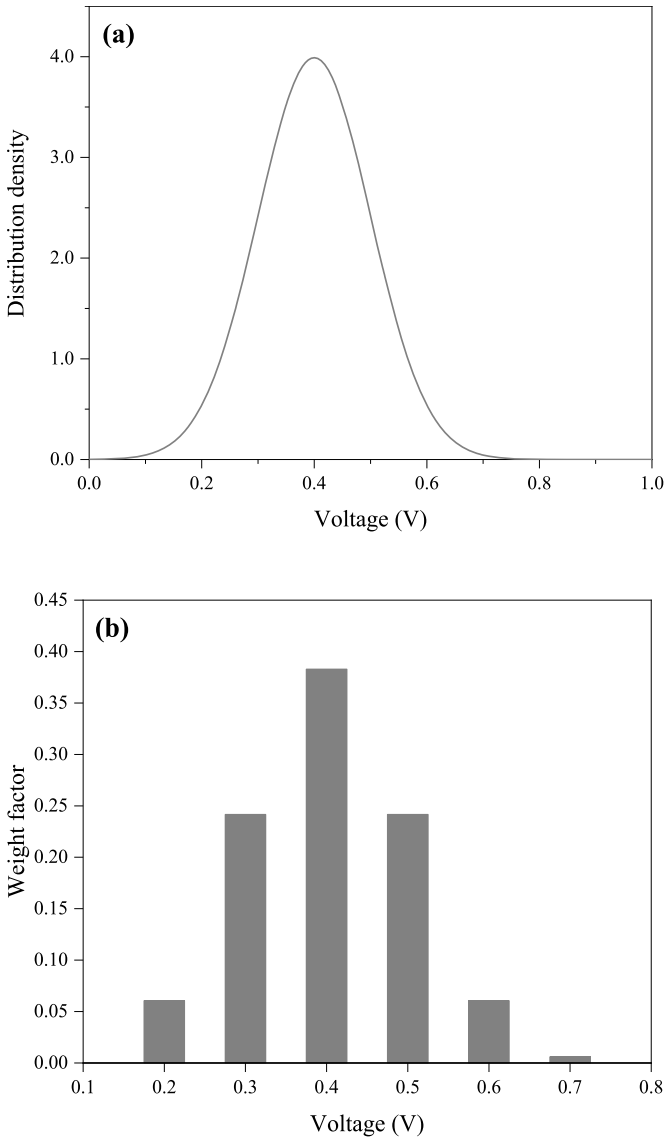

Fig. 4. The (a) distribution density and (b)weight factor of each loading voltage when the fluctuation var is 0.1.

parameter settings and the computational tolerance was set to be physics-controlled with a relative tolerance of 0.001. An in-house code based on Python platform was developed to perform ANN simulations and a commercial software, Design Expert 10, was employed for RSM models. The database was established through solving the physics-based model, which was then divided into a training set and a test set. The former and the latter accounts for 85% and 15% respectively. Firstly, ANN modelling tasks were accomplished this database, and extra data-training to improve the accuracy of ANN model was supplemented. Then the ANN models were established based on 46 and 114 data

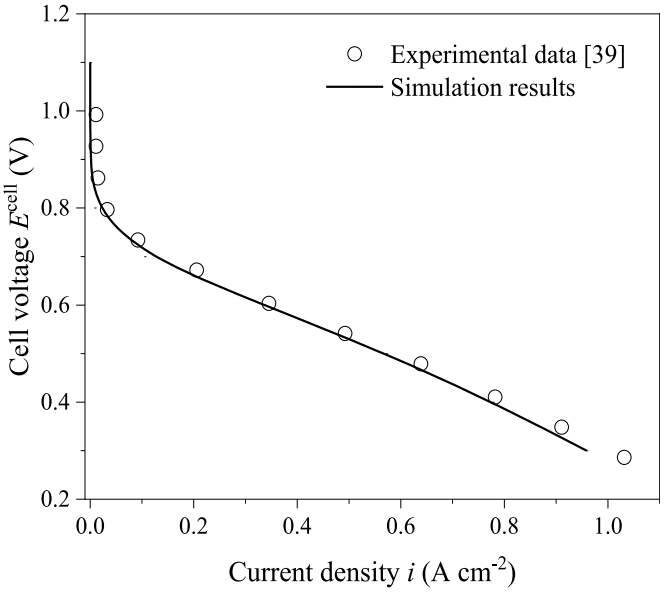

Fig. 5. Comparison of experiment data and physics-based modelling results [39].

samples, named ANN_{46} and ANN_{114}. For comparison, polynomial expressions for the relationships of design variables and objective functions were constructed through Box-Behnken Design (BBD) approach based on leave-one-out (LOO) cross-validation in the design of experiment (DoE). Polynomial terms with a p-value larger than 0.05 were considered to be insignificant and were deleted from the polynomial expressions.

2.9. Design variables and objective functions

Before the Optimization results discussed, the statement about the optimized dimensions, base-case, and parameter boundary should be set. Five parameters of GDL considered here are the compression ratio (CR), porosity (ε^0_{GDL}), compression area ratio (S_r), thickness (δ^0_{GDL}), electrical conductivity (σ^0_{GDL}) of the GDL, the base-case of which is 0.20, 0.78, 1.0, 200 μm, 12,113 S m^{-1}, respectively. The parameters' optimized ranges are detailed in Table 1. Meanwhile, the output current density and the standard deviation of oxygen distribution are taking as optimization objects.

However, in actual practice scenario, the voltage loading could hardly be kept constantly. Therefore, customization for specific operating condition was well took into account by a Gaussian weight factor: voltage fluctuation var. Then we take such a specific condition when the fluctuation of the voltage loading var is 0.1 as an example. The distribution density and the weight factors of each loading voltage, which is the section integration of the former, are shown in Fig. 4. A comprehensive fitness function, well considering the loading voltage fluctuation, was formed by Gaussian weighting the fitness at each loading voltage.

3. Results and discussion

3.1. Model validation

The physics-based model is validated by the experimental data in Fig. 5, and it is clearly indicated that the experimental polarization curve is highly consistent with the modelling results. The average deviation of the current density is only 0.01 A cm^{-2} at 0.4 V, which proves the reliability of further research of the non-uniform deformation of GDL on various transport parameters, the associated cell performance and the

Table 2
Values of used parameters in base-case and model validation conditions.

Symbol	Description (unit)	Base case	Validation case
δ^0_{GDL}	Initial GDL thickness (μm)	200	250
δ^0_{CL}	CL thickness (μm)	11.2	10
δ_M	Membrane thickness (μm)	55	55
ε^0_{GDL}	Initial GDL porosity	0.78	0.78
T	Operating temperature (K)	343.15	333.15
p	Operating pressure (atm)	1.0	1.0
RH	Relative humidity	100%	100%
α_c	Cathode transfer coefficient	0.9	0.9
σ^0_{GDL}	GDL intrinsic conductivity (S/m)	12,113	12,113
σ^0_{CL}	CL intrinsic conductivity (S/m)	450	450
W_{ch}	Channel width (mm)	1.50	1.50
W_{rib}	Rib width (mm)	1.50	1.50
CR	Compression ratio	0.20	0
E	Young's modulus (MPa)	14.0	–

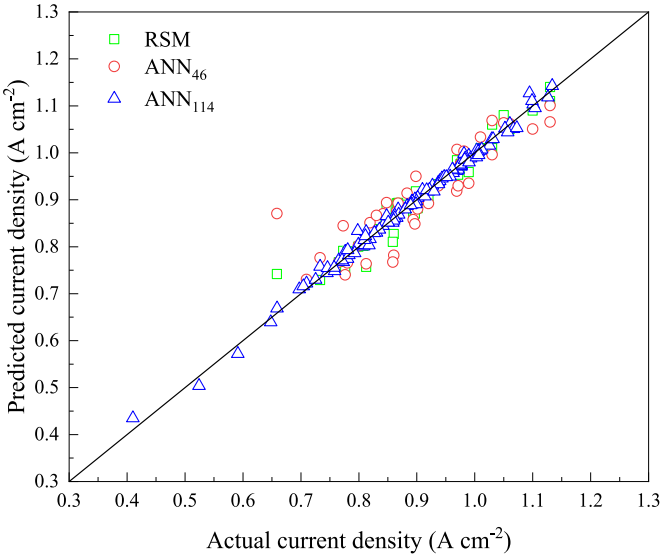

Fig. 6. Validation of current densities obtained from ANN_{46}, ANN_{114}, and RSM models at 0.4 V.

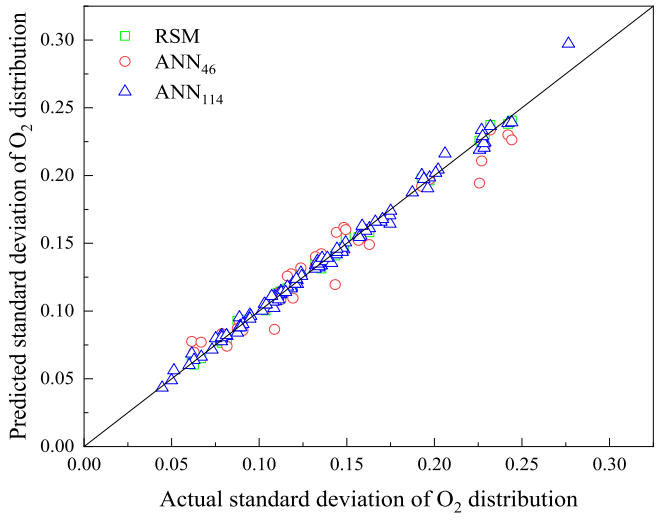

Fig. 7. Validation of oxygen homogeneities obtained from ANN_{46}, ANN_{114}, and RSM models at 0.4 V.

oxygen distribution at the boundary between GDL and CL. The

Table 3
R^2 and RMSE of predicted current density with two data-driven algorithms.

***E* (V)**	RSM		ANN_{46}		ANN_{114}	
	R^2_{pre}	RMSE	R^2_{pre}	RMSE	R^2_{pre}	RMSE
0.7	0.846	0.001	0.841	0.006	0.993	0.002
0.6	0.820	0.004	0.826	0.017	0.993	0.005
0.5	0.814	0.007	0.812	0.030	0.994	0.007
0.4	0.821	0.010	0.830	0.041	0.994	0.009
0.3	0.830	0.017	0.857	0.050	0.994	0.012
0.2	0.838	0.021	0.863	0.059	0.995	0.014
Means	0.828	0.010	0.838	0.034	0.994	0.008

Table 4
R^2 and RMSE of predicted oxygen distribution homogeneity with two data-driven algorithms.

***E* (V)**	RSM		ANN_{46}		ANN_{114}	
	R^2_{pre}	RMSE	R^2_{pre}	RMSE	R^2_{pre}	RMSE
0.7	0.994	0.002	0.958	0.006	0.995	0.002
0.6	0.996	0.002	0.967	0.007	0.994	0.003
0.5	0.991	0.003	0.974	0.007	0.994	0.004
0.4	0.989	0.004	0.966	0.009	0.993	0.004
0.3	0.985	0.004	0.951	0.010	0.992	0.004
0.2	0.979	0.005	0.953	0.011	0.991	0.005
Meanssw	0.989	0.003	0.961	0.008	0.993	0.004

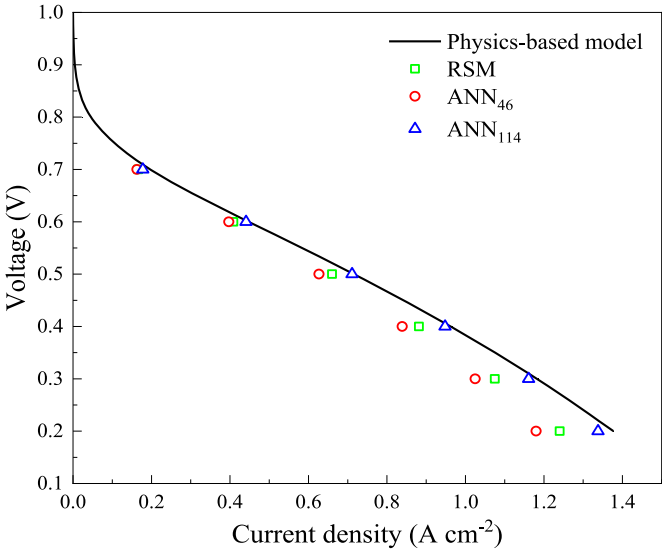

Fig. 8. Polarization curves obtained from physics-based and data-driven models in base-case condition.

parameters of validation-case and base-case can be seen in Table 2.

The test set data is used to evaluate the data-driven surrogate models. Taking the cell operating voltage at 0.4 V as examples, the predictions of the cell performances and the standard deviation of oxygen distribution (SDO2) made by ANN, RSM surrogate models and the physics-based model are illustrated in Figs. 6 and 7. The data plots under other operating voltages, i.e., 0.2 and 0.6 V are shown in Figs. S1 and S2 in the SI. For each point in the scatter diagram, the *x*-coordinate is the predicted values by the data-driven model, and the *y*-coordinate is the actual values obtained from the physics-based model in the test set database. Thus, the closer a point is to the light blue slash "$y = x$", the closer the predicted value is to the true value. Then, the validity of the model can be expressed by the correlation coefficient (R^2_{pre}) of the scatter to the "$y = x$" oblique line. As shown in Table 3, the means of R^2_{pre} of RSM, ANN_{46}, and ANN_{114}, considering the predicted current densities at all sampled operating voltages from 0.2 to 0.7 V, are 0.828, 0.838, 0.994,

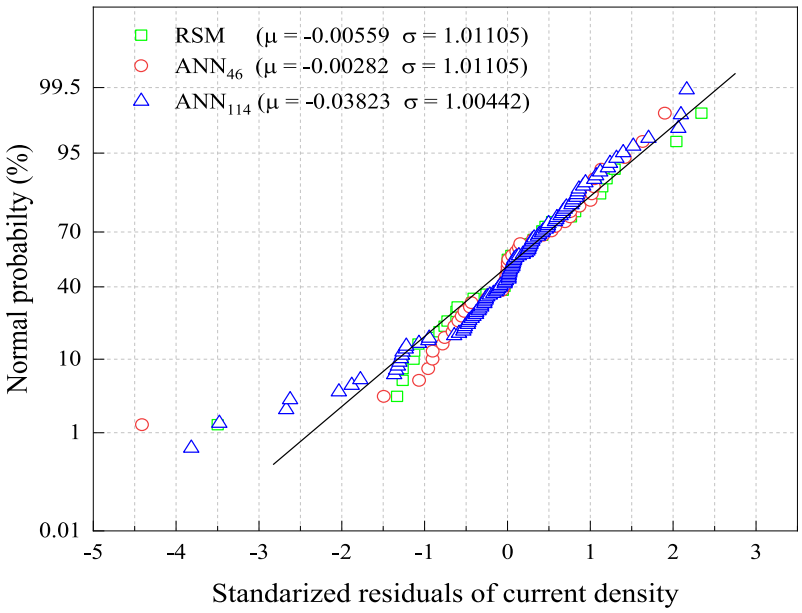

Fig. 9. Distribution of residuals of current density at 0.4 V.

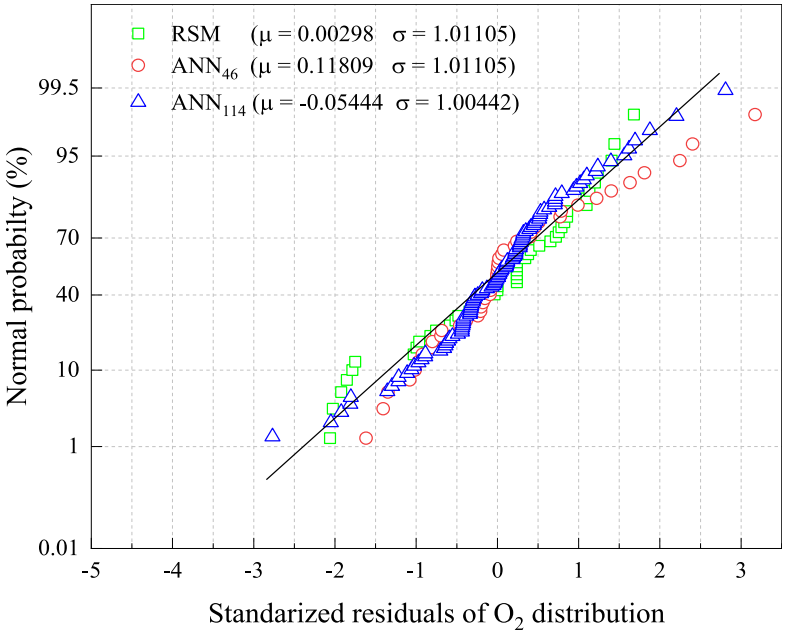

Fig.10. Distribution of residuals of the standard deviation of oxygen distribution at 0.4 V.

respectively. The average root mean squared error (RMSE) are 0.010, 0.034, 0.008, respectively. It is easy to conduct that all the three data-driven models are accurate and efficient for database learning. The data correlation recognition ability of ANN is higher than RSM owing to its higher R^2_{pre}, and it could be greatly improved by increasing the amount of data appropriately. However, the prediction error of ANN_{46} is higher than RSM. With a larger training database, the RSME of ANN_{114} decreases, indicating a better performance of the ANN_{114} model than RSM. This phenomenon could be further demonstrated by the regression results of O_2 distribution, where ANN_{46} is the worst model, and with the extended database, the average R^2 and RSME of ANN_{114} reach an extremely great lever, 0.993 and 0.004, respectively, shown in the Table 4.

As shown in Fig. 8, the polarization curves of all the studied models are compared. The average deviation of the current density is 0.02, 0.13, and 0.09 A cm^{-2} at 0.4 V with respect to ANN_{114}, ANN_{46} and RSM, respectively, which demonstrates that the physics-based model could be replaced by the data-driven models, especially the ANN_{114} model. Meanwhile, the RSM approach perform better in this task than the ANN method, as indicated by its lower prediction error, when 46 sample points are used for model training. But with a larger number of training data, the comparison result reverses. Considering the interpretability and the compatibility with the optimization algorithms, such as GA and PSO, ANN algorithm is a superior choice for further parametric optimization. The base-case parameters can be seen in Table 2.

3.2. Residual analysis

Residual analysis is accomplished to eliminate the interference of system error. The residual distributions of current density and standard

Table 5
Optimization results through RSM model.

	CR	ε^0_{GDL}	S_r	δ^0_{GDL}	σ^0_{GDL}	i at 0.4 V (A cm^{-2})	SDO_2 at 0.4 V
Base-case	0.200	0.780	1.0	200.0	12,113	0.968	0.177
Best-case 1	0.245	0.780	1.246	135.7	94,225	1.151	–
Best-case 2	0.082	0.863	0.584	387.5	49,180	–	0.062
Improvement						18.9%	65.0%

Note: Best-case 1 is the optimal case for the maximum current density; Best-case 2 is the optimal case for the most homogeneous oxygen distribution.

deviation oxygen distribution at 0.4 V, obtained from the three data-driven surrogate models, are shown in Figs. 9 and 10. The results show that the residuals of both RSM and ANN obey Gaussian distribution (also can be found in Fig. S3 in SI). It means that the systematic bias could be neglected. The average values of standardized residuals of the RSM, ANN_{46} and ANN_{114} models are -0.00559, -0.00282, -0.0382, respectively, all of which are very closely to zero. It shows that the ANN_{46} and ANN_{114} perform better the RSM. The standard deviation of the residuals of the three models are 1.011, 1.011, 1.004, respectively. It implies that the accidental errors of the models are all acceptable and ANN_{114} perform the best. Similar results could be concluded from the residual analysis on standard deviation of oxygen distribution. The residual analysis further ensures the correctness and reliability of the data-driven models, that is the basis for the subsequent discussions. The residual analyses at other cell voltages are shown in Figs. S4 and S5 in the SI, where similar findings are concluded.

3.3. Optimization

Traditionally, by mathematical means, the RSM regression functions could be quickly analysed, and the optimal combinations of studied design variables are obtained as listed in Table 5. Taking 0.4 V as an example, when CR is 0.245, ε^0_{GDL} is 0.780, S_r is 1.246, δ^0_{GDL} is 135.7 μm,

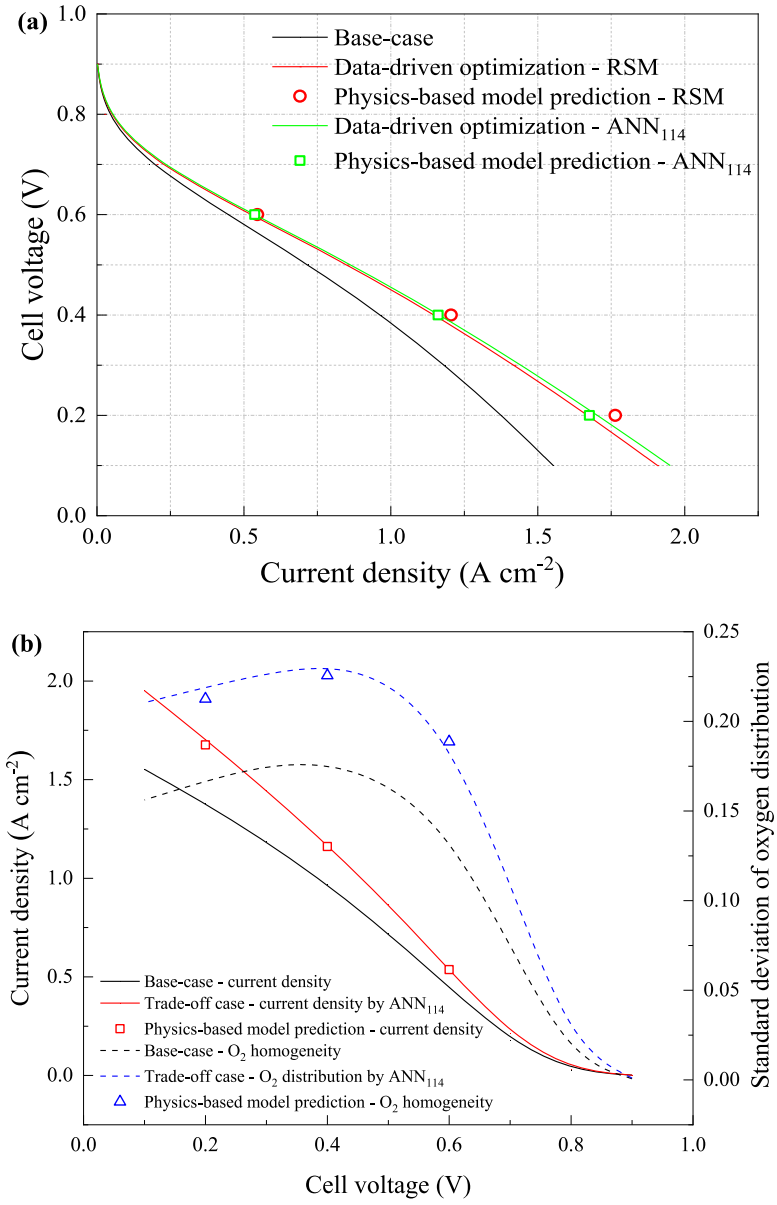

Fig. 11. The performance of the cell on base-case versus (a) best current density RSM and ANN_{114} optimization result, (b) best current density and O_2 distribution ANN_{114} optimization result.

Table 6
Optimization results through ANN model.

	CR	ε^0_{GDL}	S_r	δ^0_{GDL}	σ^0_{GDL}	i at 0.4 V (A cm^{-2})	SDO_2 at 0.4 V
Base-case	0.200	0.780	1.000	200.0	12,113	0.968	0.177
Best-case 1	0.250	0.872	0.916	100.0	95,000	1.169	–
Best-case 2	0.250	0.500	0.500	400.0	95,000	–	0.045
Improvement						20.8%	74.6%

Note: Best-case 1 is the optimal case for the maximum current density; Best-case 2 is the optimal case for the most homogeneous oxygen distribution.

σ^0_{GDL} is 94,225 S m^{-1}, the fuel cell achieves the maximum current density of 0.968 A cm^{-2}, which is a 18.9% improvement in comparison with the base-case condition. When CR, ε^0_{GDL}, S_r, δ^0_{GDL} and σ^0_{GDL} are 0.082, 0.863, 0.584, 387.5 μm, and 49,180 S m^{-1}, respectively, the most uniform oxygen distribution is achieved. In this case, the standard deviuation of oxygen distribution decreases more than 65.0% compared with the base-case condition.

To further verify the optimized parameter-combination form the RSM surrogate model, the optimized parameter-combination is verified by the physics-based model. As shown in the Fig. 11(a), the predicted results from the surrogate models (red lines) are highly consistent with the results obtained by solving the physics-based model (black circles). After optimization, the cell performance is improved compared with the base-case condition (black lines). The small errors between the optimized results from the surrogate models and physics-based model show that the optimal values of the design variables are reliable for further experimental investigation.

Advanced population optimization algorithms, e.g., GA, PSO, DE, output similar results by conducting random-selected scanning. That means the computational time and resource in this step could be greatly saved. After population initialization, the population constantly changes the search directions through their own experience and the experience of others. Adaptive research rules are always inspired by bionics or other fields. Finally, the optimal fitness and corresponding conditions are determined by judging whether the optimization termination requirements are met. This replaces the inefficient exhaustive global scanning of engineers in the face of high-dimension and high-complexity engineering optimization problems, accelerates the optimization progress, and improves the accuracy and reliability of the conclusions. Then, the fitness function of cell performance (current density) or oxygen distribution (standard deviation of the oxygen profile) are established and optimized to adapt to different application scenarios or application requirements. DE is sifted by its obviously lower efficient. Considering the generational decrease of GA and PSO for the cell performance optimization at 0.4 V, as shown in Fig. S6 in the SI, PSO is selected to conduct the optimization task.

Defining the current density and standard deviation of oxygen dis-

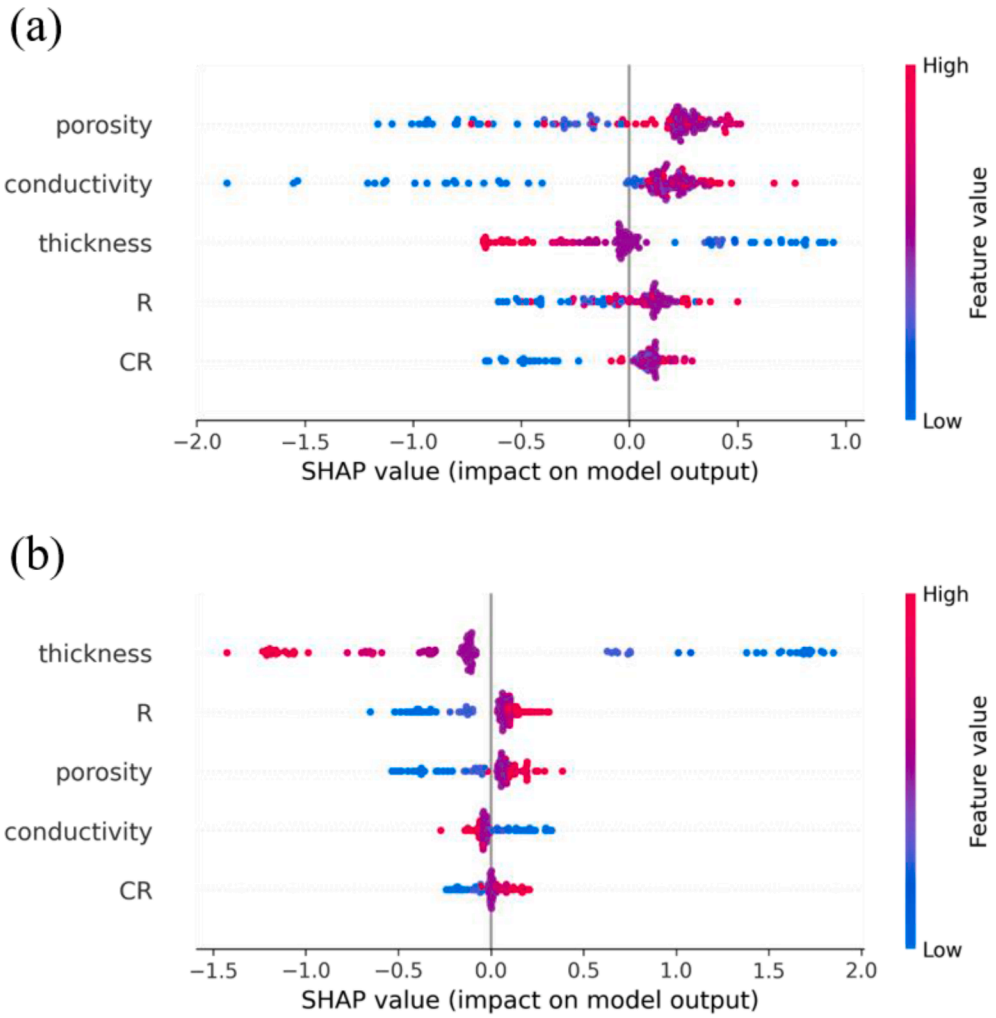

Fig. 12. The feature-importance of each parameter on (a) the current density at 0.4 V and (b) the O_2 distribution at 0.4 V by the ANN_{114} regression analysis model.

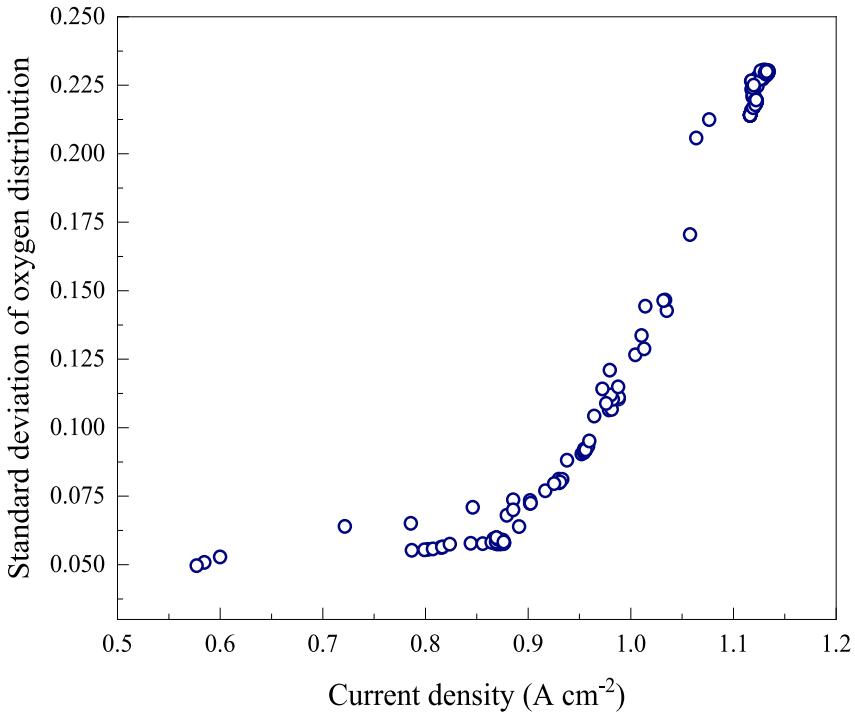

Fig. 13. Multi-object optimization results conducted by PSO algorithm.

tribution as the optimization fitness functions, respectively, as shown in Table 6, after PSO optimization, the fuel cell achieves the best performance at 0.4 V when *CR*, ε^0_{GDL}, S_r, δ^0_{GDL} and σ^0_{GDL} are 0.250, 0.872, 0.916, 100.0 μm, and 95,000 S m^{-1}, respectively. The best current density is 1.169 A cm^{-2} and the corresponding standard deviation of oxygen distribution homogeneity is 0.23 at 0.4 V. The cell performance is improved by 20.8% compare with the base-case condition. The highest oxygen distribution homogeneity is obtained when CR, ε^0_{GDL}, S_r,δ^0_{GDL} and σ^0_{GDL} are 0.250, 0.500, 0.500, 400.0 μm, and 95,000 S m^{-1}, respectively. The standard deviation of oxygen distribution decreases over 74.6% compared with the base-case condition.

The optimized results predicted by the ANN model are also verified by the physics-based model, as shown in Fig. 12(a), indicating that the accuracy of the ANN model is higher.

Based on above analysis, it is found that the current density is very low, e.g., 0.59 A cm^{-2} at 0.4 V, when the most homogeneous oxygen distribution is achieved, that can be explained by the relatively slower electrochemical reaction rate. As shown in Fig. 12, the effect-visualizations of each parameter by SHAP, an AI model analysis tool, on the ANN_{114} data-driven model easily differentiate the functional rule of each parameter at 0.4 V. The totally different feature-importance ranking and the final optimized results demonstrated the two considered objects are conflicted with each other, which is also confirmed by the results at other operating cell voltages (see Fig. S7 in SI). It means that the situation cannot be both performance-excellent and oxygen distribution-homogeneous. Therefore, an approach, considering both, give the best parameter combination is more practically meaningful. The multi-objective optimization process was conducted by PSO with a comprehensive optimization object formed by linear weight the performance and oxygen distribution, as illustrated in Fig. 13. GA and DE also achieve very similar results compared with PSO (see Fig. S8 in SI). It is easily to balance the need of oxygen distribution homogeneity and the weighted current density by adjusting the weight ratio of the optimized objects. Then the corresponding parameter combination could be obtained. It would be very convenient for engineering workers to adjust the linear weight factors to balance the two key objects when it is needed. Taking the occasion when linear weight factor is 0.5 as an example,

Table 7
Maximize current density improvement simultaneously by ANN model.

	CR	ε^0_{GDL}	S_r	δ^0_{GDL}	σ^0_{GDL}	0.4 V (A cm^{-2})	0.4 V SDO_2
Base-case	0.200	0.780	1.000	200.0	12,113	0.968	0.177
Trade-off case	0.158	0.807	0.931	100.0	95,000	1.166	0.223
Improvement						20.5%	−26.0%

Note: The trade-off case is the weight factor of 0.5 for the two objectives.

through PSO algorithms, as shown in Table 7, the fuel cell meets the best-balanced performance when *CR*, ε^0_{GDL}, S_r, δ^0_{GDL} and σ^0_{GDL} are 0.158, 0.807, 0.931, 100.0 μm, 95,000 S m^{-1} at 0.4 V. At this cell voltage, the current density is 1.166 A cm^{-2} and the corresponding standard deviation of oxygen distribution homogeneity is 0.223. The current density is improved by 20.5% and the standard deviation of oxygne distribution increases more than 26.0% compared with the base-case condition.

The optimized parameter-combination From ANN_{114} model could be further validated by the physical-based model, shown in the Fig. 11 (b), where the prediction oxygen distribution and current density from ANN_{114} and the simulated results of physical-based model keep highly consistent. The errors are acceptable for further experiment guidance.

4. Conclusions

To accurately address the fully coupled complex chemical-physical processes occurred in PEM fuel cells and solve the traditional time-consuming and economically unfordable multi-variable and multi-objective optimization of GDL, physics-based simulation and machine-learning-based surrogate modelling are integrated to build a sophisticated M^5 model, in which multi-physics and multi-phase flow simulation, machine-learning-based surrogate modelling, multi-variable and multi-objects optimization are included, to accelerate the optimization of the deformed GDL of PEMFCs. The main contribution of this paper is concluded following:

a) Considering the non-uniform deformation of GDL, a physics-based model and two data-driven models (RSM and ANN) are established. The data-driven models are proven accurate to replace the physics-base model for the quicker analysis and optimization of five key design variables of the GDL.
b) The RSM method can obtain polynomial expressions between design variables and objective functions. The accuracy of RSM is higher than ANN models when the sample points are small (such as 46). However, the prediction accuracy of ANN model is superior to that of RSM after increasing the number of training samples.
c) Two objective functions, i.e., current density (cell performance) and the standard deviation of oxygen distribution (reaction homogeneity), are optimized. After optimization, the former is improved by 20.8% and the latter is decreased by 74.6%, respectively.
d) Pareto front is obtained to present the trade-offs of the two objective functions. When each of the two objectives has a weight factor of 0.5, the current density increases by 20.5% while sacrificing 26.0% of the standard deviation of oxygen distribution.

Declaration of Competing Interest

The authors declare that they have no known competing financial interests or personal relationships that could have appeared to influence the work reported in this paper.

Data availability

Data will be made available on request.

Acknowledgement

The authors acknowledge the financial support from National Natural Science Foundation of China (21978118).

Supplementary materials

Supplementary data associated with this article can be found, in the online version, at 10.1016/j.egyai.2023.100261.

References

[1] St-Pierre J, Wilkinson DP. Fuel cells: a new, efficient and cleaner power sources. AIChE J 2001;47:1482–6.
[2] Wang Y, Chen KS, Mishler J, Cho SC, Adroher XC. A review of polymer electrolyte membrane fuel cells: technology, applications, and needs on fundamental research. Appl Energy 2011;88:981–1007.
[3] Debe MK. Electrocatalyst approaches and challenges for automotive fuel cells. Nature 2012;486:43–51.
[4] Weber A, Borup RL, Darling RM, Das PK, Dursch TJ, et al. A critical review of modeling transport phenomena in polymer-electrolyte fuel cells. J Electrochem Soc 2014;161:F1254–99.
[5] Raissi M, Yazdani A, Karniadakis GE. Hidden fluid mechanics: learning velocity and pressure fields from flow visualizations. Science 2020;367:1026–30.
[6] Wang Y, Seo B, Wang B, Zamel N, Jiao K, Adroher XC. Fundamentals, materials, and machine learning of polymer electrolyte membrane fuel cell technology. Energy and AI 2020;1:100014.
[7] Song G-H, Meng H. Numerical modeling and simulation of PEM fuel cells: progress and perspective. Acta Mech Sinica-Prc 2013;29:318–34.
[8] Demuren A, Edwards RL. Modeling proton exchange membrane fuel cells - A Review. 50 years of CFD in engineering sciences. Springer; 2020. p. p513–47.
[9] Zhang GB, Yuan H, Wang Y, Jiao K. Three-dimensional simulation of a new cooling strategy for proton exchange membrane fuel cell stack using a non-isothermal multiphase model. Appl Energy 2019;255:113865.
[10] Schneider P, Sadeler C, Scherzer A-N, Zamel N, Gerteisen D. Fast and reliable state-of-health model of a PEM cathode catalyst layer. J Electrochem Soc 2019;166:F322–33.
[11] Wang B, Zhang G, Wang H, Xuan J, Jiao K. Multi-physics-resolved digital twin of proton exchange membrane fuel cells with a data-driven surrogate model. Energy and AI 2020;1:100004.
[12] Gu GH, Noh J, Kim I, Jung Y. Machine learning for renewable energy materials. J Mater Chem A 2019;7:17096–117.
[13] Fanourgakis GS, Gkagkas K, Tylianakis E, Froudakis GE. A universal machine learning algorithm for large-scale screening of materials. J Am Chem Soc 2020;142:3814–22.
[14] Khajeh-Hosseini-Dalasm N, Ahadian S, Fushinobu K, Okazaki K, Kawazoe Y. Prediction and analysis of the cathode catalyst layer performance of proton exchange membrane fuel cells using artificial network and statistical methods. J Power Sources 2011;196:3750–6.
[15] Ding R, Ding Y, Zhang H, Wang R, Xu Z, et al. Applying machine learning to boost the development of high-performance membrane electrode assembly for proton exchange membrane fuel cells. J Mater Chem A 2021;9:6841–50.
[16] Moein-Jahromi M, Kermani MJ. Three-dimensional multiphase simulation and multi-objective optimization of PEM fuel cells degradation under automotive cyclic loads. Energy Convers Manag 2021;231:113837.
[17] Ma R, Yang T, Breaz E, Li Z, Boris P, Gao F. Data-driven proton exchange membrane fuel cell degradation prediction through deep learning method. Appl Energy 2018;231:102–15.
[18] Chang CC, Lin CJ. LIBSVM: a library for support vector machines. ACM Trans Intell Syst Technol (TIST) 2011;2:27–32.
[19] ANSYS fluent advanced add-on modules. Canonsburg, PA, USA: ANSYS Inc; 2016.
[20] Sacks J, Welch WJ, Mitchell TJ, Wynn HP. Design and analysis of computer experiments. Stat Sci 1989;4:409–23.
[21] Secanell M, Karan K, Suleman A, Djilali N. Multi-variable optimisation of PEMFC cathodes using an agglomerate model. Electrochimi Acta 2007;52:6318–37.
[22] Sun W, Peppley BA, Karan K. An improved two-dimensional agglomerate cathode model to study the influence of catalyst layer structural parameters. Electrochimi Acta 2005;50:3359–74.
[23] Secanell M, Songprakorp R, Suleman A, Djilali N. Multi-objective optimization of a polymer electrolyte fuel cell membrane electrode assembly. Energy Environ. Sci. 2008;1:378–88.
[24] Secanell M, Songprakorp R, Djilali N, Suleman A. Optimisation of a proton exchange membrane fuel cell membrane electrode assembly. Struct Multidisc Optim 2010;40:563–83.
[25] Khajeh-Hosseini-Dalasm N, Fesanghary M, Fushinobu K, Okazaki K. A study of the agglomerate catalyst layer for the cathode side of proton exchange membrane fuel cell: modelling and optimization. Electrochim Acta 2012;60:55–65.
[26] Xing L, Song X, Scott K, Pickert V, Cao W. Multi-variable optimization of PEMFC cathodes based surrogate modelling. Int J Hydrogen Energy 2013;38:14295–313.
[27] Wang B, Xie B, Xuan J, Jiao K. AI-based optimization of PEM fuel cell catalyst layers for maximum power density via data-driven surrogate modeling. Energy Convers Manag 2020;205:112460.
[28] Ding R, Yin W, Cheng G, Chen Y, Wang J, Wang R, Rui Z, Li J, Liu J. Boosting the optimization of membrane electrode assembly in proton exchange membrane fuel cells guided by explainable artificial intelligence. Energy and AI 2021;5:100098.
[29] Silva RE, Gouriveau R, Jemei S, Hissel D, Boulon L, Agbossou K, Yousfi Steiner N. Proton exchange membrane fuel cell degradation prediction based on adaptive neuro-fuzzy inference systems. Int J Hydrogen Energy 2014;39:11128–44.
[30] Chen G, Xu Q, Xuan J, Liu J, Fu Q, Shi W, Su H, Xing L. Numerical study of inhomogeneous deformation of gas diffusion layers on proton exchange membrane fuel cells performance. J Energy Storage 2021;44:103486.
[31] Moein-Jahromi M, Kermani MJ. Three-dimensional multiphase simulation and multi-objective optimization of PEM fuel cells degradation under automotive cyclic loads. Energy Conver Manage 2021;231:113837.
[32] Kamarajugadda S, Mazumder S. Numerical investigation of the effect of cathode catalyst layer structure and composition on polymer electrolyte membrane fuel cell performance. J Power Sources 2008;183(2):629–42.
[33] Shah AA, Kim GS, Sui PC, Harvey D. Transient non-isothermal model of a polymer electrolyte fuel cell. J Power Sources 2007;163(2):793–806.
[34] Xing L, Xu Y, Penga Ž, Xu Q, Su H, Shi W, Barbir F. A novel flow field with controllable pressure gradient to enhance mass transport and water removal of PEM fuel cells. AIChE J 2020;66(6).
[35] Xing L, Mamlouk M, Scott K. A two dimensional agglomerate model for a proton exchange membrane fuel cell. Energy 2013;61:196–210.
[36] Pasaogullari U, Wang C-Y. Two-phase transport and the role of micro-porous layer in polymer electrolyte fuel cells. Electrochim Acta 2004;49(25):4359–69.
[37] Sun W, Peppley BA, Karan K. An improved two-dimensional agglomerate cathode model to study the influence of catalyst layer structural parameters. Electrochim Acta 2005;50(16):3359–74.
[38] Wilke CR. A viscosity equation for gas mixture. J Chem Phys 1950;18:517e9.
[39] Xing L, Liu X, Alaje T, Kumar R, Mamlouk M. A two-phase flow and non-isothermal agglomerate model for a proton exchange membrane (PEM) fuel cell. Energy 2014;73:618–34.
[40] Zhang H, Rahman MA, Mojica F, Sui PC, Chuang PYA. A comprehensive two-phase proton exchange membrane fuel cell model coupled with anisotropic properties and mechanical deformation of the gas diffusion layer. Electrochim Acta 2021;382:138273.
[41] Zhou P, Wu CW, Ma GJ. Contact resistance prediction and structure optimization of bipolar plates. J Power Sources 2006;159(2):1115–22.
[42] Xing L, Xu Y, Penga Ž, Xu Q, Su H, Barbir F, et al. A segmented fuel cell unit with functionally graded distributions of platinum loading and operating temperature. Chem Eng J 2021;406:126889.